




Effect of hydrogen-related shallow donor on the physical and chemical properties of Ag-doped ZnO nanostructures

Qais M. Al-Bataineh^{1,2,3}, Riad Ababneh⁴, A. Bahti^{1,3}, Areen A. Bani-Salameh², Carlos J. Tavares⁵, and Ahmad Telfah^{1,4,*} 

¹Leibniz Institut für Analytische Wissenschaften-ISAS-e.V., Bunsen-Kirchhoff-Straße 11, 44139 Dortmund, Germany

²Department of Physical Sciences, Jordan University of Science & Technology, P.O. Box 3030, Irbid 22110, Jordan

³Experimental Physics, TU Dortmund University, 44227 Dortmund, Germany

⁴Department of Physics, Yarmouk University (YU), Irbid 21163, Jordan

⁵Centre of Physics of Minho and Porto (CF-UM-PT) Universities, University of Minho, 4804-533 Guimarães, Portugal

Received: 29 March 2022

Accepted: 1 June 2022

Published online:

15 July 2022

© The Author(s) 2022

ABSTRACT

Silver-doped zinc oxide nanostructures (Ag/ZnO NSs) with Ag content of 0 wt%, 5 wt%, 10 wt%, and 20 wt% were synthesized using a hydrothermal technique. The prepared nanostructures were annealed at 500 °C for 2 h. The samples were characterized by using scanning electron microscopy, FTIR, X-ray diffraction (XRD), and electrical conductivity. FTIR spectra confirms the presence of hydrogen-related shallow donor defects in the Ag/ZnO NSs, which bind to the oxygen vacancy (H_O) and consequently plays a significant role in the physicochemical properties of the metal oxide nanostructures. The H_O defects are blended to O- and Zn-polar Ag-doped ZnO NSs, depending on their polarity. XRD results verified that Ag/ZnO NSs have a polycrystalline hexagonal structure. Williamson–Hall methods were used to estimate the microstructural properties of polycrystalline nanostructures. The electrical conductivity increased from 0.60 to 1.10 $\mu\text{S}/\text{cm}$, and the bandgap energy decreased from 3.36 to 3.10 eV by increasing the Ag from 0 wt% up to 20 wt%.

1 Introduction

Zinc oxide nanoparticles (ZnO NPs) are attractive semiconductors because of their excellent physical properties, such as n-type semiconductors, excellent optical and electronic properties, high electronic mobility, fast recombination of electron–hole pairs,

excellent photocatalytic activity, high thermal conductivity, and limited visible light absorbance [1, 2]. The bandgap energy and exciton binding energy of the ZnO NPs are 3.37 eV and 60 meV, respectively [2, 3]. ZnO has a stable wurtzite hexagonal structure with lattice constants $a = 3.250 \text{ \AA}$ and $c = 5.207 \text{ \AA}$ [4]. According to these properties, ZnO NPs are used in

Address correspondence to E-mail: telfah.ahmad@isas.de

different applications, such as solar cells [5], optoelectronic devices [6], gas sensors [7], biosensors [8], light-emitting devices [9], and photocatalysis [10]. Many physical and chemical parameters control the synthesis of the ZnO NPs size and morphology, such as solvent pH [11], synthesized solvents [12], annealing temperature [13], and dopant materials [14].

Therefore, the dopant materials and concentrations affect ZnO nanostructures' physical and chemical properties [15–17]. Among the dopant materials, silver (Ag) is used as a dopant material for zinc oxide nanostructures (ZnO NSs) to improve physical and chemical properties since Ag has high chemical stability and high electrical conductivity [18]. Many studies focused on investigating the influence of Ag doping in ZnO nanostructures. For instance, O. Yildirim et al. [19] confirm that silver has a high affinity in substituting Zn^{2+} ions in the crystal lattice and consequently affects the inclusion of energetic states within ZnO, which leads to a decrease in the bandgap energy. In addition, P. Panchal et al. [20] confirm that the Ag/ZnO nanostructures with 1.0 wt% of Ag have a good photocatalytic and antimicrobial activity compared to pure ZnO NPs. Moreover, doping ZnO nanostructures by Ag changes the optical absorption toward the red region, decreasing the bandgap energy and consequently increasing the photocatalytic and antibacterial activity [21].

The hydrogen impurity forms shallow donor defects in the ZnO structure, affecting the optical, optoelectronic, and electrical properties of ZnO [22–25]. This work is focused on the influence of hydrogen-related shallow donor defects in addition to Ag concentration as a dopant material on the chemical, structural, and morphological properties of Ag/ZnO NSs. FTIR absorbance spectra were studied to investigate the hydrogen-related shallow donor defects in the Ag/ZnO NSs. In addition, the X-ray diffraction (XRD) technique is a crucial characterization tool that provides essential information about crystal phase, crystalline structure, crystallinity degree, and microstructural properties for bulk, thin films, and nanostructures. According to the definition of the perfect crystal extended in all directions to infinity, there is no perfect crystal infinite size. Therefore, the nanostructures are not perfect crystals and consequently have a broadening of the diffraction peaks. All microstructural properties of the nanostructure are extracted from the peak linewidth

analysis [26]. After growing the nanostructure and before studying the physical properties, XRD characterization should be studied to identify the microstructural properties that affect all physical properties, such as optical, electrical, and electronic properties. Moreover, the effect of Ag doping and hydrogen-related shallow donor defects on the optical, optoelectronic, and electrical properties of Ag/ZnO NSs were investigated.

2 Experimental set-up and sample preparation

Ag/ZnO NSs (0, 5, 10, and 20 wt%) were synthesized by the hydrothermal method. An amount of 5 g zinc acetate dihydrate ($Zn(CH_3CO_2)_2 \cdot 2H_2O$) and (0, 0.25, 0.5, and 1) g silver nitrate ($AgNO_3$) were dissolved in 50 mL absolute ethanol in the beaker (1) and then placed in a water bath at 70 °C. At the same time, an amount of 1.25 g of sodium hydroxide (NaOH) was dissolved in 50 mL of absolute ethanol in a beaker (2). The solution (2) was dropped into the beaker (1) at a rate of 10 mL/min. The resultant solution was kept in a water bath for 2 h at 70 °C. The obtained Ag/ZnO NSs were washed with ethanol and distilled water. The Ag/ZnO NSs were dried in an oven at 90 °C for 24 h, and then, later on, Ag/ZnO NSs were annealed at 500 °C for 2 h to remove defects [25].

The structural and morphological properties of Ag/ZnO NSs were investigated using X-ray diffraction (XRD) analysis (Malvern Panalytical Ltd, Malvern, UK) and scanning electron microscopy (SEM) (FEI Quanta FEG 450). Fourier transform infrared spectroscopy (Bruker Tensor 27 spectrometer) investigated the chemical structure. UV/Vis spectrophotometer (U-3900 H) and 4-point probe (Microworld Inc.) connected with a high-resolution multimeter (Keithley 2450 Sourcemeter) were used to investigate the optical and electrical properties.

3 Results and discussion

3.1 Morphological properties and surface wettability

SEM results show that undoped ZnO NPs exhibit a hexagonal structure with an average size between 30 and 40 nm (Fig. 1a). The morphological structure was

transferred from particles to uniform rods in Ag/ZnO NSs (Fig. 1b–d). Ag/ZnO NSs average particle sizes at 5, 10, and 20 wt% are in the range of 30–40 nm.

ZnO NPs and Ag/ZnO NSs surface wettability were investigated between surface and water droplets through static water contact angle (WCA) measurements (Fig. 2). The average WCA of ZnO NPs is 35°, while it was 49° for Ag/ZnO NSs indicating a significant increase in surface hydrophobicity associated with the transforming from the nanoparticle phase (ZnO NSs) to the nanorod phase (Ag/ZnO NSs).

3.2 Chemical structure

The absorbance band in ZnO NPs of stretching Zn–O bonds appears between 500 and 750 cm^{-1} , and the absorbance band of bending O–H bonds appears between 800 and 1000 cm^{-1} (Fig. 3). Moreover, the absorbance band of stretching O–H bonds appears at 3340 cm^{-1} . Moreover, the peaks at 1360 cm^{-1} are attributed to the acetate group, the residual from

Fig. 1 SEM micrographs of Ag/ZnO NSs with Ag contents of **a** 0 wt%, **b** 5 wt%, **c** 10 wt%, and **d** 20 wt%

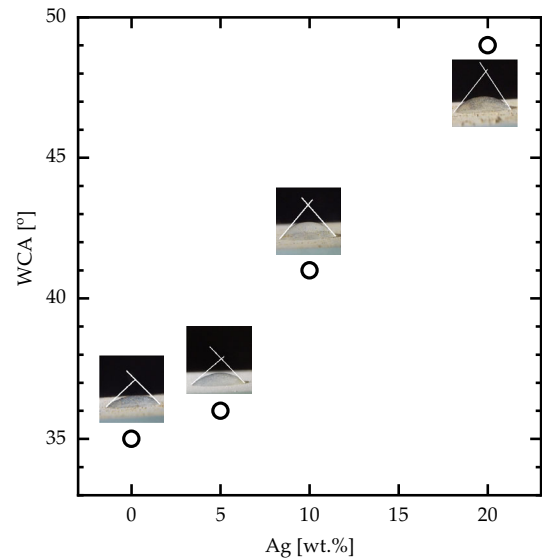
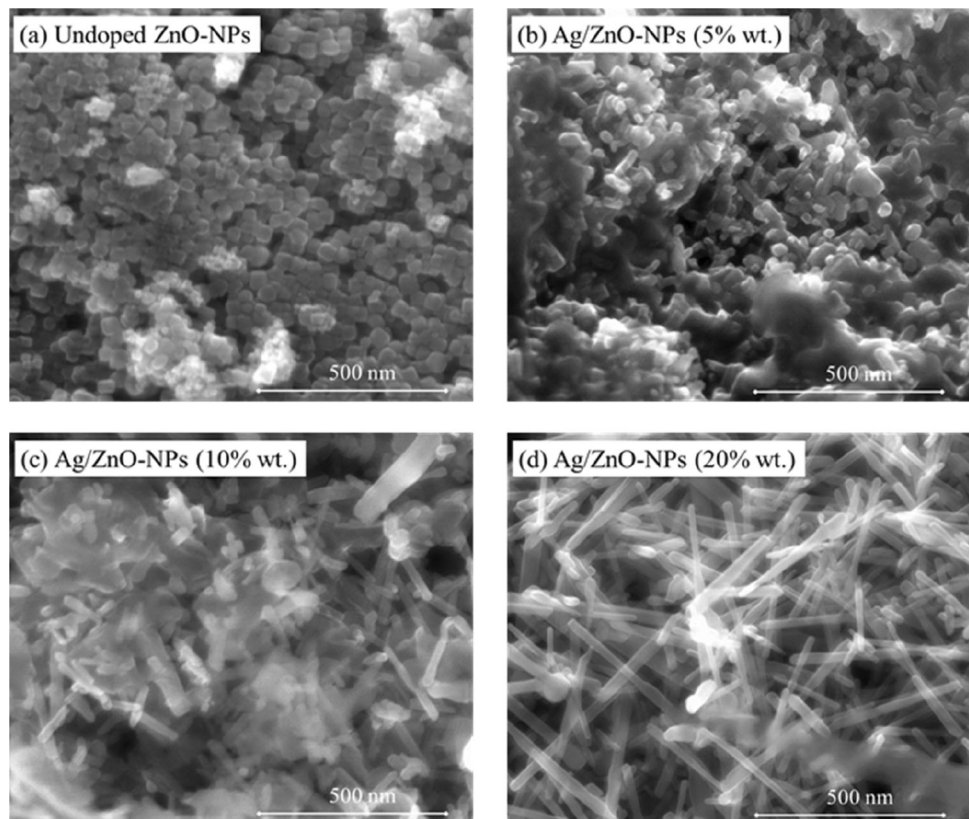


Fig. 2 Contact angle of Ag/ZnO NSs (Ag contents of 0, 5, 10, and 20 wt%)

starting material used for preparing ZnO NPs [27]. A new band appeared at 1120 cm^{-1} in Ag/ZnO NSs attributed to the Ag–O bonds. The existence of stretching O–H bonds in Ag/ZnO NSs at 3340 cm^{-1} , which annealed at 500 °C without an external H

source, shows an H-containing defect in the nanostructures. This suggests the existence of hydrogen-related shallow donors in the Ag/ZnO NSs, which bounds to the oxygen vacancy (H_O), [28]. More important, hydrogen-related shallow donor defects with multiple O–H bonds in a zinc vacancy in the form of H_O are expected to play an essential role in the physicochemical properties of the metal oxide nanostructures [29]. According to our published article, the formation and dissociation of the O–H bonds depend on the annealing temperature and time [30]. According to C. Van de Walle’s study [31], the H^+ ions have a low enough formation energy to induce their high solubility in ZnO due to the great strength of the O–H bond. The H_O defects are blended to O- and Zn-polar Ag-doped ZnO NSs, depending on their polarity.

3.3 Crystal structure

All microstructural properties of the nanostructure are extracted from the peak linewidth analysis [26]. Moreover, microstructural characterizations, such as

crystalline domain size (D), microstrain (ϵ), internal lattice strain (σ), and other parameters were also investigated using Williamson–Hall (WH) method and its modifications. Figure 4 illustrates the XRD pattern of the Ag/ZnO NSs. The powder XRD pattern was indexed using qualitative phase analysis software (Qualx2). The XRD diffraction peaks for undoped ZnO NSs are detected at 31.60° , 34.27° , 36.10° , 47.39° , 56.45° , 62.73° , 67.82° , and 68.95° , corresponding to the Miller indices of (100), (002), (101), (102), (2–10), (103), (200), and (2–12), respectively, being well-matched for a standard hexagonal wurtzite ZnO with the space group of P63mc according to the JCPSD card no. 036-1451 and 071-3830. Introducing Ag into the ZnO NSs is found to lead to giving rise to additional peaks at 38.03° , 44.22° , 64.37° , and 77.30° corresponding to the Miller indices of Ag(111), Ag(200), Ag(220), Ag(311), respectively [32]. At the same time, no other crystal phases are identified in the patterns for all samples indicating a high degree of purity. Figure 4 also confirms the hexagonal ZnO phase formation and the presence of cubic Ag phase, which means that the quantity of Ag reaches the solubility limit [33].

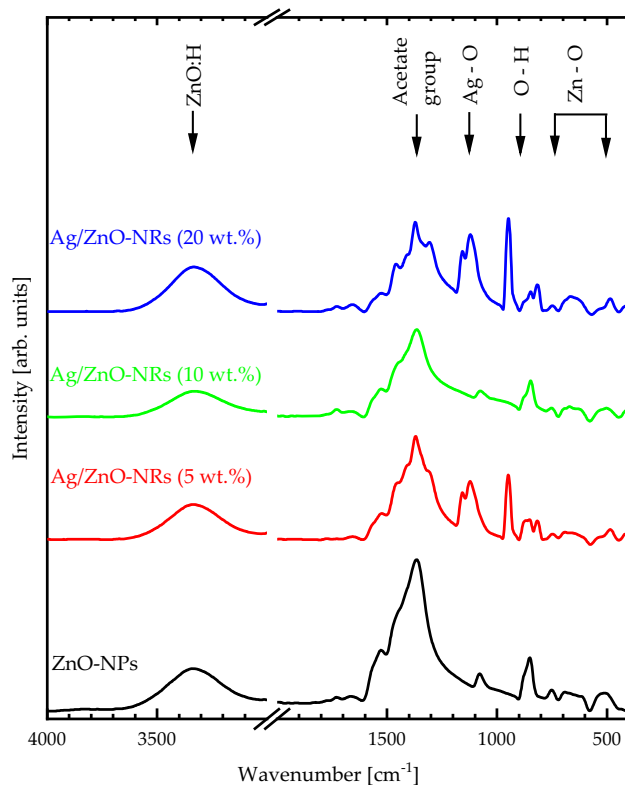


Fig. 3 FTIR spectra of Ag/ZnO NSs at Ag content of 0, 5, 10, and 20 wt%

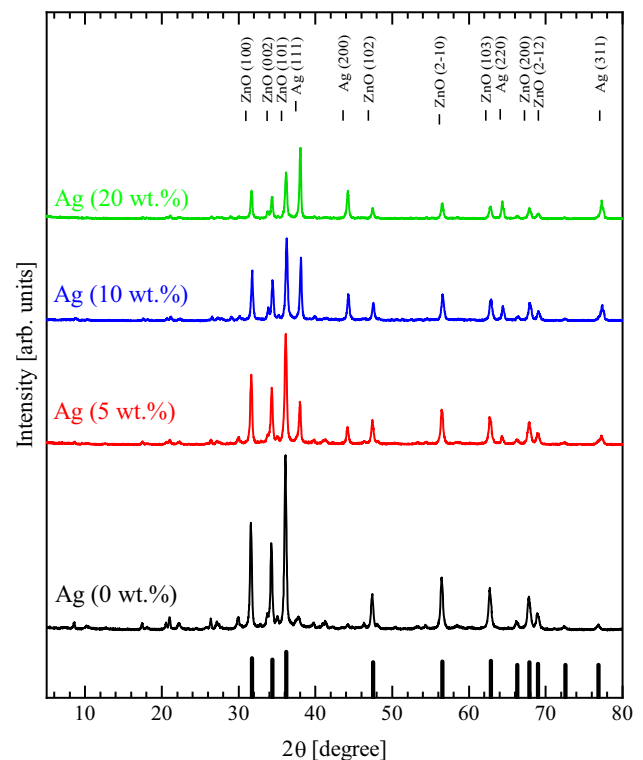


Fig. 4 XRD patterns of Ag/ZnO NSs at Ag content of 0, 5, 10, and 20 wt%

By increasing the Ag content, the main orientations of the ZnO structure along with (100), (002), and (101) atomic planes were decreased in intensity and shifted to higher Bragg angles (Fig. 4). This means that Ag doping decreases the crystallinity and consequent increases the microstrain of Ag/ZnO NSs, which results from the stresses induced by the ionic radii difference of Zn and Ag ions and subsequent changing the crystal plane polarity of Ag/ZnO NSs [34].

The crystallinity degree ($X_{\text{cryst}}\%$) which is the ratio between the integrated area under the diffraction peaks (A_{crys}) to the total area ($A_{\text{crys}} + A_{\text{amorph}}$) was calculated (Table 1) according to the following equation [35]:

$$X_{\text{cryst}}\% = \frac{A_{\text{crys}}}{A_{\text{crys}} + A_{\text{amorph}}} \times 100\%. \quad (1)$$

The crystallinity degree of the undoped ZnO NPs is 64.71%. Increasing Ag content in Ag/ZnO NSs decreases the crystallinity degree. The lattice constants are determined by indexing the diffraction peaks from different reflections for polycrystalline nanostructures. Accordingly, the lattice constants and other related parameters of Ag/ZnO NSs were studied. All Ag/ZnO NSs were found to have a polycrystalline hexagonal structure. According to JCPDS card no. 036-1451 and 071-3830, the lattice constants of the ZnO hexagonal structure are $a_0 = b_0 = 3.2489 \text{ \AA}$ and $c_0 = 5.2068 \text{ \AA}$. Firstly, the

interplanar space d_{hkl} values are estimated according to Bragg's law ($n\lambda = 2d_{hkl} \sin \theta_{hkl}$) [36, 37], where n is an integer, λ is the wavelength of X-ray ($\lambda = 1.54184 \text{ \AA}$), and θ is the angle of incidence.

After determining the diffraction angle, (hkl) values, and the d_{hkl} for the main three peaks in the XRD pattern of Ag/ZnO NSs in Fig. 4, the lattice constants and the unit cell volume (v) of Ag/ZnO NSs were calculated (Table 1) from the standard formula of the hexagonal structure as $a = \sqrt{4/3}d_{100}$, $c = 2d_{002}$, and $v = 0.866a^2c$, respectively. It is worth mentioning that the atomic and ionic radii of Zn^{+2} are 1.42 Å and 1.35 Å, while Ag^+ are 1.75 Å and 1.15 Å, respectively [38]. Moreover, the variations in the lattice constant values are due to the insertion of the Ag ion in interstitial positions of the ZnO wurtzite cell [38].

There is a slight difference between the measured lattice constants and standard lattice constants for the ZnO wurtzite structure, indicating the existence of internal stress in the NSs. As shown in Sect. 3.2, the presence of hydrogen-related shallow donors is the main reason for the internal stress in Ag/ZnO NSs, which binds to the oxygen vacancy, H_O which leads to defects formation, including multiple O–H bonds in a zinc vacancy. Therefore, the average internal stress (σ) along the x-axis and z-axis of Ag/ZnO NSs were determined (Table 1) using Eqs. 3 and 4, respectively [39]:

Table 1 The structural and microstructural parameters of Ag/ZnO NSs determined by using XRD

Parameters	Symbol and Unit	Ag (0 wt%)	Ag (5 wt%)	Ag (10 wt%)	Ag (20 wt%)
Degree of crystallinity	$X_{\text{crys}}\%$	64.71%	59.68%	55.03%	48.69%
Lattice constants	a [Å]	3.27	3.27	3.26	3.26
	c [Å]	5.24	5.23	5.21	5.22
c/a	c/a	1.60	1.60	1.60	1.60
Unit cell volume	v [Å ³]	48.51	48.34	47.83	48.17
In-plane average internal stress (a)	σ_a [GPa]	− 0.139	− 0.107	− 0.011	− 0.075
Out-of-plane average internal stress (c)	σ_c [GPa]	− 0.144	− 0.116	− 0.034	− 0.090
UDM	D [nm]	37	34	36	35
	$\langle \epsilon \rangle \times 10^{-3}$	1.23	1.19	1.05	0.86
USDM	$\delta \times 10^{-11}$ line/cm ²	1.69	0.88	0.79	0.80
	σ [GPa]	0.177	0.171	0.151	0.124
UEDDM	D [nm]	37	34	35	35
	σ [GPa]	0.149	0.144	0.129	0.108
	u [MJ m ^{−3}]	0.109	0.102	0.079	0.054

$$\sigma_a = \frac{E}{2\gamma} \left(\frac{a_0 - a}{a_0} \right) \tag{2}$$

$$\sigma_c = \frac{E}{2\gamma} \left(\frac{c_0 - c}{c_0} \right), \tag{3}$$

where E and γ are Young modulus and the Poisson ratio of Ag/ZnO NSs, respectively.

The main microstructural analysis parameter depends on the diffraction peak linewidth at half maximum (FWHM, β). The linewidth observed (β_{Obs}) is the superposition between the linewidth of the sample (β_{hkl}) and the linewidth of the instruments or the silicon standard (β_{Ins}). There are many reasons for the microstrain formation in the nanostructures, such as points and planes defects, and the grain boundaries [40, 41].

Williamson–Hall (WH) method is a reliable method used to investigate the crystallite size, microstrain, and other microstructural properties of the nanostructures. This method also proposes that the linewidth of the XRD peaks affects the microstructural properties, particularly the particle size [26, 42]. The total linewidth of the XRD peaks (β_{total}) composed of superposition of the particle size linewidth (β_{size}) and microstrain linewidth (β_{strain}) is derived according to [33]

$$\beta_{\text{total}} = \beta_{\text{size}} + \beta_{\text{strain}}. \tag{4}$$

Parameters D and $\langle \varepsilon \rangle$ of the Ag/ZnO NSs were investigated using modified forms of the WH equation, such as the uniform deformation model (UDM), uniform stress deformation model (USDM), and uniform deformation energy density model (UEDM) [35, 43]. UDM considers the microstrain linewidth of the XRD peaks resulting from the defects in the crystal, which can be imperfections [32]. The variation of the D and $\langle \varepsilon \rangle$ depends on $1/\cos\theta$ and $\tan\theta$, respectively. Moreover, the total linewidth of a diffraction peak with Miller indices (hkl) is given by [44]

$$\beta_{\text{hkl}} \cos\theta = \frac{k\lambda}{D} + 4\langle \varepsilon \rangle \sin\theta \tag{5}$$

This model supposes that the strain is uniform in all directions and consequently supposes that the crystal has an isotropic nature. Figure 5a illustrates $\beta_{\text{hkl}}\cos\theta$ plotted versus $4\sin\theta$ of Ag/ZnO NSs. The points were fit fairly to linear function fit with an average R^2 of 81.80%. From the fit results, the slope

represents the $\langle \varepsilon \rangle$, and the y-intercept represents D value in average. The average D and $\langle \varepsilon \rangle$ that deduced from the UDM as explained above are listed in Table 1. It is observed that D and $\langle \varepsilon \rangle$ decreases with the increase in Ag content, associated to the change in the crystallization of Ag/ZnO NSs [32].

USDM considers the lattice deformation stress along with all plane directions, which means that nanostructures have an anisotropic and inhomogeneous nature [32, 45–47]. Therefore, WH equations are modified depending on Hooke’s law, which states that the stress (σ) relates to the microstrain $\langle \varepsilon \rangle$, according to the following relation $\sigma = \langle \varepsilon \rangle \times Y_{\text{hkl}}$, where Y_{hkl} is elastic Young modulus [47, 48]. Consequently, Eq. (6) was rearranged as [35, 43]

$$\beta_{\text{hkl}}\cos\theta = \frac{k\lambda}{D} + \frac{4\sigma}{Y_{\text{hkl}}} \sin\theta. \tag{6}$$

Moreover, the Young modulus for hexagonal structure is given by [49, 50]

$$Y_{\text{hkl}} = \frac{\left(h^2 + \frac{(h+2k)^2}{3} + \left(\frac{a_0l}{c_0} \right)^2 \right)^2}{S_{11} \left(h^2 + \frac{(h+2k)^2}{3} \right)^2 + S_{33} \left(\frac{a_0l}{c_0} \right)^2 + (2S_{13} + S_{44}) \left(h^2 + \frac{(h+2k)^2}{3} \right) \left(\frac{a_0l}{c_0} \right)^2}, \tag{7}$$

where S_{ij} are elastic compliances. According to Eq. (7), the slope of the linear fit function gives the σ value, while the y-intercept represents the average D value. Table 1 shows the average D and σ that are estimated from the USDM.

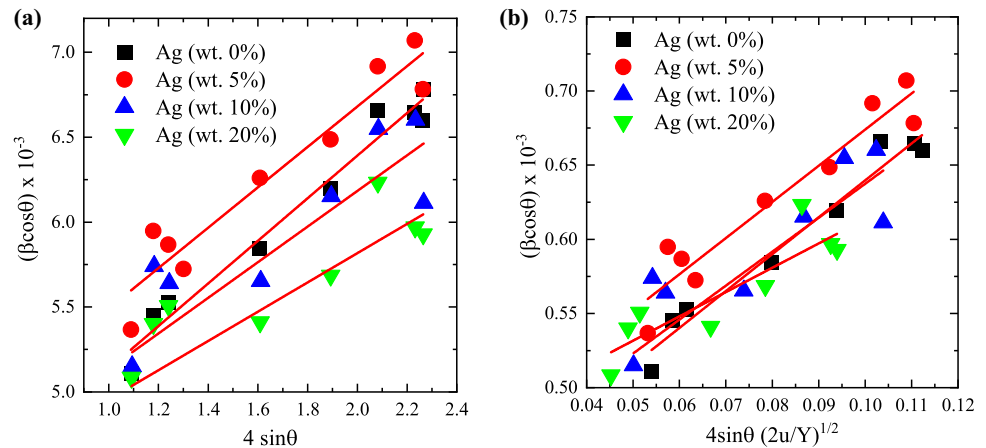
UEDM considers that the nanostructure has regular anisotropic nature in all directions due to the deformation energy density [51]. The energy density (u) can be related with the strain by $u = \langle \varepsilon^2 \rangle Y/2$ [46]. Therefore, the $\langle \varepsilon \rangle$ values are reformulated as $\langle \varepsilon \rangle = \sigma \sqrt{2u/Y}$. Substituting by $\langle \varepsilon \rangle$ values into Eq. (7) [52],

$$\beta_{\text{hkl}} \cos\theta = \frac{k\lambda}{D} + 4\sigma \sin\theta \sqrt{\frac{2u}{Y}}. \tag{8}$$

Plotting $\beta_{\text{hkl}} \cos\theta$ against $4\sin\theta(2u/Y)^{1/2}$ gives the D values from the intercept and the σ values from the slope, while the u values calculated from $u = \langle \varepsilon^2 \rangle Y/2$ (Fig. 5b). Table 1 shows the average D , σ , and u estimated from the UEDM.

A dislocation is an atomic line imperfection in the nanostructures due to the existence of internal stresses. Moreover, the dislocation density is considered the main category of crystalline defects, which

Fig. 5 **a** UDM and **b** UDEDM plots of the Ag/ZnO NSs (Ag content: 0, 5, 10, and 20 wt%)



influences the nanostructure stiffness, strength, rigidity, and ductility [53]. The dislocation density depends on the crystallite size, the formation of the crystal, and morphological properties. Williamson–Smallman equations are used to estimate the dislocation density of the nanostructures as [54]

$$\delta = 1/D^2. \quad (9)$$

The values of dislocation density of the Ag-doped ZnO NSs according to the crystallite size deduced from the WH method are listed in Table 1. The δ -value for ZnO NPs is 1.69×10^{-11} line/cm² and decreases as Ag content is increased in Ag/ZnO NSs, indicating the decrease in the imperfections accordingly.

3.4 Optical properties

The transmittance spectra of pure ZnO NPs have a sharp increase in the transmittance values from 0 to 88% as an incident photon wavelength increases from 300 to 400 nm, and no changes can be observed in the range of 400–700 nm (Fig. 6a). The electrons in the valance band of ZnO NPs required high incident photon energy (UV-light) to break and transport them to the conduction bands. Therefore, the ZnO NPs have high transmittance values between 400 and 700 nm, which means that there are no free electrons in the ZnO structure. Doping ZnO NSs by Ag decreases the transmittance values in the incident photon wavelength range of 400–700 nm because the Ag⁺ ions contain free electrons, which can absorb incident photons with lower energy and consequently transport them to higher energy (Fig. 6b). Moreover, shifting the absorption edge to the low energy region

indicate that the increase in Ag concentrations has led to decrease the bandgap energy (Fig. 6a).

The extinction coefficient is a factor that represents the amount of light absorption in the material, calculated by the equation $k = \alpha\lambda/4\pi$, where α is the absorption coefficient, given by $\alpha = (1/d)\ln[(1-R)/T]$ [55]. The higher values of the k -spectra of Ag/ZnO NSs below the incident photon wavelength of 350 nm are attributed to the absorption light by electron to transit from valance and conduction bands. While for incident photon wavelengths above 350 nm, the k -values of Ag/ZnO NSs are low, which means that the Ag-doped ZnO NSs permit passing the EM photons through the film with low photons decaying or damping. In addition, the increase in Ag dopant concentration in ZnO NSs leads to an increase in the k -values, due to absorbing incident photons by the free electrons due to the doping (Fig. 6c).

The refractive index (n) spectra of Ag/ZnO NSs were investigated using the equation $n = (1 + R/1 - R) + \sqrt{(4R/(1 - R)^2) - k^2}$ [55]. The n -spectra of the ZnO NPs (Fig. 6d) exhibit two behaviors the anomalous behavior ($250 \leq \lambda < 400$ nm), which represents many photon–matter interactions, such as, photon absorption due to the electronic transition, and the resonance effect resulting from the equality of the incident photon frequency and the plasma frequency [56]. The normal behavior ($400 \leq \lambda < 700$ nm) represents the normal decrease of the refractive index.

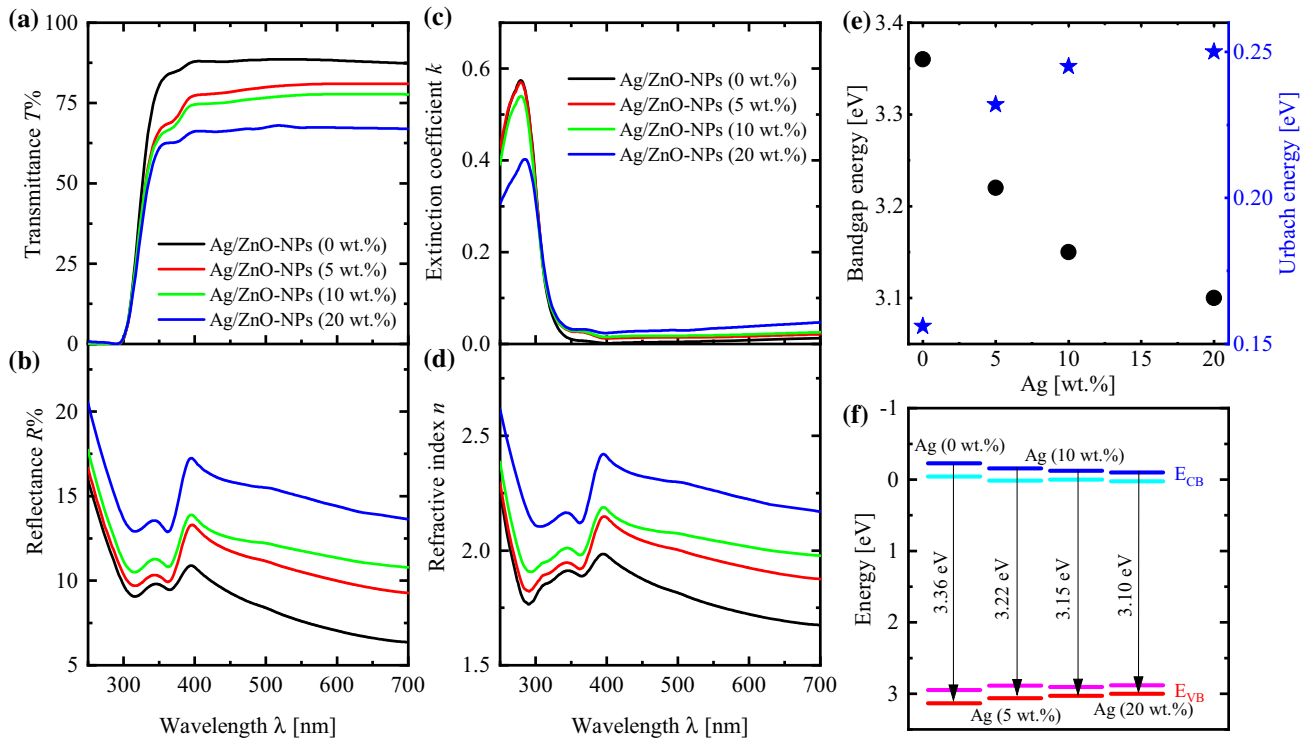


Fig. 6 **a** Transmittance, **b** reflectance, **c** extinction coefficient, **d** refractive index spectra of Ag/ZnO NSs, **e** bandgap energy and Urbach energy of Ag-doped ZnO NSs as a function of Ag

concentration, and **f** schematic diagram of the band structure for Ag/ZnO NSs at Ag content of 0, 5, 10, and 20 wt%

Bandgap energies (E_g) of Ag/ZnO NSs were calculated by plotting $(\alpha hv)^2$ versus hv , according to the Tauc equation $(\alpha hv)^2 = \beta(hv - E_g)$. In addition, the substates between the valance (VB) and conduction (CB) bands resulting from the disorder in Ag/ZnO NSs were studied using the Urbach energy (E_U) by the equation $\alpha = \alpha_0 \exp(hv/E_u)$ [57]. The E_g and E_U values for ZnO NPs are 3.36 eV and 0.16 eV, respectively. Ag concentration increase into Ag/ZnO NSs was led to decrease E_g and increase E_U values (Fig. 6e), because of the strong interaction between the d-element of Ag^+ ion and s- and p-electrons of the ZnO. The interchange in sp-d electrons in the Ag/ZnO NSs generates new energy levels between the valance and conduction bands due to the disorder in the nanostructures [34]. This leads to an increase in localized state density in the mobility bandgap of the Ag/ZnO NSs [58]. The resulting band structure, including the E_{VB} , E_{CB} , bandgap energy, and the substates were investigated using the ionization energy and the electron affinity energy, according to the literature [59, 60]. The schematic diagram of band structure for Ag-doped ZnO NSs illustrates the

decrease in the E_{CB} , and the increase in the E_{VB} with the increase in Ag content supporting the decrease in E_g accordingly (Fig. 6f).

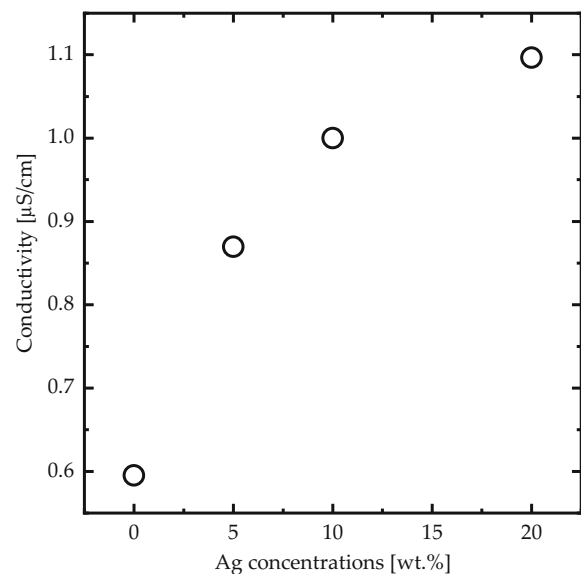


Fig. 7 Electrical conductivity of Ag/ZnO NSs at Ag concentrations of 0, 5, 10, and 20 wt%

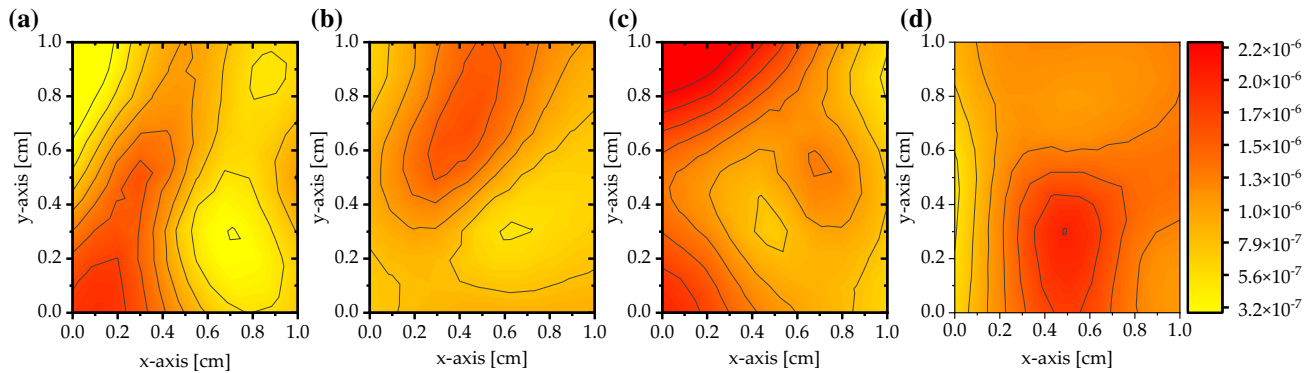


Fig. 8 The conductivity mapping (1 cm × 1 cm) of Ag/ZnO NSs at **a** 0 wt%, **b** 5 wt%, **c** 10 wt%, and **d** 20 wt%

3.5 Electrical properties

The electrical conductivity in composite films depends on many parameters, including dopant type, dopant concentration, and crystallinity degree of the material [61]. Figure 7 illustrates the electrical conductivity values for the Ag/ZnO NSs as a function of Ag concentrations. The electrical conductivity of the pure ZnO NPs is related to the existence of carrier density of O- and Zn-polar due to the formation of hydrogen-related shallow donor defects. In addition, O-vacancies, Zn-interstitials and the hydrogen-related shallow donor are the origins of the n-type of undoped ZnO NPs [29]. The electrical conductivity of the Ag/ZnO NSs increases from 0.60 to 1.10 $\mu\text{S}/\text{cm}$ with increasing Ag concentrations up to 20 wt%. In addition, the conductivity mapping of ZnO NPs (Fig. 8a) shows a variation of the conductivity across the film surface, which can be attributed to the growth process, the quality of the transfer process, and other parameters. The increase in Ag content has led to an increase in the variation in the conductivity across the film surface of Ag/ZnO NSs (Fig. 8b–d).

4 Conclusions

Doping ZnO NPs with Ag has led to the formation of Ag/ZnO NSs and to transform the nanostructure morphological from nanoparticles to nanorods and to increase the surface hydrophobicity. The resultant average size after doping was between 30 and 40 nm.

FTIR spectra of Ag/ZnO NSs confirm the presence of hydrogen-related shallow donors, which binds to the oxygen vacancy, H_O . The H_O defects are blended to O- and Zn-polar Ag/ZnO NSs, depending on their polarity. X-ray diffraction experiments verified that Ag/ZnO NSs have a polycrystalline hexagonal structure. The stress and strain deduced from the Williamson–Hall (WH) method refer to the hydrogen-related shallow donors in Ag/ZnO NSs that are bound to the oxygen vacancy, H_O . The electrical conductivity increased from 0.60 to 1.10 $\mu\text{S}/\text{cm}$, and the bandgap energy decreased from 3.36 to 3.10 eV by increasing the Ag content from 0 wt.% up to 20 wt.% due to generating new energy levels between the valence and conduction bands.

Acknowledgements

The authors would like to acknowledge Jordan University of Science and Technology. Our thanks also to Prof. Ahmad A. Ahmad and Prof. Mohammad-Ali H. Al-Akhras for helping our members to use thin films and biomedical laboratories.

Author contribution

QMA-B: conceptualization, methodology, writing—original draft. RA: data acquisition, writing—review and editing. AB: preparation, data acquisition. AAB-S: preparation, data acquisition. CJT: conceptualization, writing—review and editing. AT: conceptualization, supervision, writing—review and editing.

Funding

Open Access funding enabled and organized by Projekt DEAL. Financial Support by the Ministerium für Innovation, Wissenschaft und Forschung des Landes Nordrhein-Westfalen, the Senatsverwaltung für Wirtschaft, Technologie und Forschung des Landes Berlin, and the Bundesministerium für Bildung und Forschung is gratefully acknowledged.

Data availability

Not applicable.

Declarations

Conflict of interest The authors declare that they have no known competing financial interests or personal relationships that could have influenced the work reported in this paper.

Consent to participate All authors participate in this work.

Consent to publish All authors agree to publish this work.

Open Access This article is licensed under a Creative Commons Attribution 4.0 International License, which permits use, sharing, adaptation, distribution and reproduction in any medium or format, as long as you give appropriate credit to the original author(s) and the source, provide a link to the Creative Commons licence, and indicate if changes were made. The images or other third party material in this article are included in the article's Creative Commons licence, unless indicated otherwise in a credit line to the material. If material is not included in the article's Creative Commons licence and your intended use is not permitted by statutory regulation or exceeds the permitted use, you will need to obtain permission directly from the copyright holder. To view a copy of this licence, visit <http://creativecommons.org/licenses/by/4.0/>.

References

1. S. Iqbal et al., Designing highly potential photocatalytic comprising silver deposited ZnO NPs with sulfurized graphitic carbon nitride (Ag/ZnO/Sg-C₃N₄) ternary composite. *J. Environ. Chem. Eng.* **9**(1), 104919 (2021)
2. A. Alsaad, Q.M. Al-Bataineh, A. Ahmad, Z. Albataineh, A. Telfah, Optical band gap and refractive index dispersion parameters of boron-doped ZnO thin films: a novel derived mathematical model from the experimental transmission spectra. *Optik* **211**, 164641 (2020)
3. R. Rathnasekara, P. Hari, Impedance spectroscopy of nanostructured ZnO morphologies. *J. Mater. Res.* **39**, 1–11 (2021)
4. D. Norton, Y. Heo, M.P.K. Ip, S.J. Pearton, M.F. Chishoim, T. Steiner, ZnO: growth, doping & processing. *Mater. Today* **6**, 34 (2004)
5. S. Bhatt, R. Shukla, C. Pathak, S.K. Pandey, Evaluation of performance constraints and structural optimization of a core-shell ZnO nanorod based eco-friendly perovskite solar cell. *Sol. Energy* **215**, 473–481 (2021)
6. L. Chen, Z. Yin, S. Mei, X. Xiao, H.-Q. Wang, Enhanced photoelectric performance of inverted CsPbI₂Br perovskite solar cells with zwitterion modified ZnO cathode interlayer. *J. Power Sources* **499**, 229909 (2021)
7. J. Liu, L. Zhang, J. Fan, B. Zhu, J. Yu, Triethylamine gas sensor based on Pt-functionalized hierarchical ZnO microspheres. *Sens. Actuators B* **331**, 129425 (2021)
8. G.S. Mei, P.S. Menon, G. Hegde, ZnO for performance enhancement of surface plasmon resonance biosensor: a review. *Mater. Res. Express* **7**(1), 012003 (2020)
9. E. Moyen, J.H. Kim, J. Kim, J. Jang, ZnO nanoparticles for quantum-dot-based light-emitting diodes. *ACS Appl. Nano Mater.* **3**(6), 5203–5211 (2020)
10. B. Albiss, M. Abu-Dalo, Photocatalytic degradation of methylene blue using zinc oxide nanorods grown on activated carbon fibers. *Sustainability* **13**(9), 4729 (2021)
11. I. Joško, J. Dobrzyńska, R. Dobrowolski, M. Kusiak, K. Terpiłowski, The effect of pH and ageing on the fate of CuO and ZnO nanoparticles in soils. *Sci. Total Environ.* **721**, 137771 (2020)
12. T. Andelman et al., Morphological control and photoluminescence of zinc oxide nanocrystals. *J. Phys. Chem. B* **109**(30), 14314–14318 (2005)
13. Q.M. Al-Bataineh, A. Alsaad, A. Ahmad, A. Al-Sawalmih, Structural, electronic and optical characterization of ZnO thin film-seeded platforms for ZnO nanostructures: sol-gel method versus ab initio calculations. *J. Electron. Mater.* **48**(8), 5028–5038 (2019)
14. A. Alsaad, A. Ahmad, I. Qattan, Q.M. Al-Bataineh, Z. Albataineh, Structural, optoelectrical, linear, and nonlinear optical characterizations of dip-synthesized undoped ZnO and group III elements (B, Al, Ga, and In)-doped ZnO thin films. *Crystals* **10**(4), 252 (2020)

15. J. Li, X. Zhu, Q. Xie, D. Yang, Surface nanosheets evolution and enhanced photoluminescence properties of Al-doped ZnO films induced by excessive doping concentration. *Ceram. Int.* **45**(3), 3871–3877 (2019)
16. H. Wu, J. Ding, D. Yang, J. Li, Y. Shi, Y. Zhou, Graphene quantum dots doped ZnO superstructure (ZnO superstructure/GQDs) for weak UV intensity photodetector application. *Ceram. Int.* **46**(11), 17800–17808 (2020)
17. X. Zhu et al., High photoresponse sensitivity of lithium-doped ZnO (LZO) thin films for weak ultraviolet signal photodetector. *J. Alloys Compd.* **805**, 309–317 (2019)
18. F. Alzoubi et al., Physicochemical characteristics of silver nanoparticles: influence of carbonate alkalinity. *Nanotechnol. Environ. Eng.* **6**(3), 1–9 (2021)
19. Ö.A. Yıldırım, H.E. Unalan, C. Durucan, Highly efficient room temperature synthesis of silver-doped zinc oxide (ZnO:Ag) nanoparticles: structural, optical, and photocatalytic properties. *J. Am. Ceram. Soc.* **96**(3), 766–773 (2013)
20. P. Panchal, D.R. Paul, A. Sharma, P. Choudhary, P. Meena, S. Nehra, Biogenic mediated Ag/ZnO nanocomposites for photocatalytic and antibacterial activities towards disinfection of water. *J. Colloid Interface Sci.* **563**, 370–380 (2020)
21. W. Vallejo, A. Cantillo, C. Díaz-Urbe, Methylene blue photodegradation under visible irradiation on Ag-doped ZnO thin films. *Int. J. Photoenergy* (2020). <https://doi.org/10.1155/2020/1627498>
22. K. Shimomura, K. Nishiyama, R. Kadono, Electronic structure of the muonium center as a shallow donor in ZnO. *Phys. Rev. Lett.* **89**(25), 255505 (2002)
23. D.M. Hofmann et al., Hydrogen: a relevant shallow donor in zinc oxide. *Phys. Rev. Lett.* **88**(4), 045504 (2002)
24. B.K. Meyer et al., Bound exciton and donor–acceptor pair recombinations in ZnO. *Phys. Status Solidi (B)* **241**(2), 231–260 (2004)
25. F. Herklotz, E. Lavrov, V. Kolkovsky, J. Weber, M. Stavola, Charge states of a hydrogen defect with a local vibrational mode at 3326 cm^{-1} in ZnO. *Phys. Rev. B* **82**(11), 115206 (2010)
26. R. Yogamalar, R. Srinivasan, A. Vinu, K. Ariga, A.C. Bose, X-ray peak broadening analysis in ZnO nanoparticles. *Solid State Commun.* **149**, 43–44 (2009)
27. N. Akbar, Z. Aslam, R. Siddiqui, M.R. Shah, N.A. Khan, Zinc oxide nanoparticles conjugated with clinically-approved medicines as potential antibacterial molecules. *AMB Express* **11**(1), 1–16 (2021)
28. A. Janotti, C.G. Van de Walle, Hydrogen multicentre bonds. *Nat. Mater.* **6**(1), 44–47 (2007)
29. T. Cossuet, F. Donatini, A.M. Lord, E. Appert, J. Pernot, V. Consonni, Polarity-dependent high electrical conductivity of ZnO nanorods and its relation to hydrogen. *J. Phys. Chem. C* **122**(39), 22767–22775 (2018)
30. A.A. Ahmad, Q.M. Al-Bataineh, I.A. Aljarrah, A.D. Telfah, Electrochemical degradation of methyl red in zinc hydroxide and zinc oxide thin films, physical and chemical activation. *Mater. Chem. Phys.* **280**, 125793 (2022)
31. C.G. Van de Walle, Hydrogen as a cause of doping in zinc oxide. *Phys. Rev. Lett.* **85**(5), 1012 (2000)
32. D. Nath, F. Singh, R. Das, X-ray diffraction analysis by Williamson-Hall, Halder-Wagner and size-strain plot methods of CdSe nanoparticles—a comparative study. *Mater. Chem. Phys.* **239**, 122021 (2020)
33. A. Hassanien, A.A. Akl, A. Saaedi, Synthesis, crystallography, microstructure, crystal defects, and morphology of Bi x Zn 1-x O nanoparticles prepared by sol-gel technique. *CrystEngComm* **20**(12), 1716–1730 (2018)
34. A. Ahmad, A. Migdadi, A. Alsaad, Q.M. Al-Bataineh, A. Telfah, Optical, structural, and morphological characterizations of synthesized (Cd-Ni) co-doped ZnO thin films. *Appl. Phys. A* **127**(12), 1–12 (2021)
35. A.A. Akl, I. El Radaf, A.S. Hassanien, An extensive comparative study for microstructural properties and crystal imperfections of Novel sprayed Cu3SbSe3 Nanoparticle-thin films of different thicknesses. *Optik* **227**, 165837 (2021)
36. A. Ahmad, A. Alsaad, Q. Al-Bataineh, A. Bani-Salameh, H. Al-Khateeb, M. Al-Naafa, Optical and structural characterization of dip synthesized Al-B Co-doped ZnO seeded platforms for ZnO nanostructures. *Jordan J Phys.* **10**(1), 33–48 (2017)
37. W.L. Bragg, The diffraction of short electromagnetic waves by a crystal. *Scientia* **23**, 45 (1929)
38. I.S. Kim, E.-K. Jeong, D.Y. Kim, M. Kumar, S.-Y. Choi, Investigation of p-type behavior in Ag-doped ZnO thin films by E-beam evaporation. *Appl. Surf. Sci.* **255**(7), 4011–4014 (2009)
39. A.A. Akl, A.S. Hassanien, Comparative microstructural studies using different methods: effect of Cd-addition on crystallography, microstructural properties, and crystal imperfections of annealed nano-structural thin CdxZn1-xSe films. *Phys. B: Condens. Matter* **620**, 413267 (2021)
40. P. Bindu, S. Thomas, Estimation of lattice strain in ZnO nanoparticles: X-ray peak profile analysis. *J. Theor. Appl. Phys.* **8**(4), 123–134 (2014)
41. A.K. Zak, W.A. Majid, M.E. Abrishami, R. Yousefi, X-ray analysis of ZnO nanoparticles by Williamson–Hall and size-strain plot methods. *Solid State Sci.* **13**(1), 251–256 (2011)
42. R. Delhez, T.H. De Keijser, E. Mittemeijer, Determination of crystallite size and lattice distortions through X-ray diffraction line profile analysis. *Fresenius’ Z. Für Analytische Chemie* **312**(1), 1–16 (1982)

43. A.A. Akl, I.E. Radaf, A.S. Hassanien, Intensive comparative study using X-Ray diffraction for investigating microstructural parameters and crystal defects of the novel nanostructural ZnGa₂S₄ thin films. *Superlattices Microstruct.* **143**, 106544 (2020)
44. Q.M. Al-Bataineh, M. Telfah, A.A. Ahmad, A.M. Alsaad, I.A. Qattan, H. Baaziz, Z. Charifi, A. Telfah, Synthesis, crystallography, microstructure, crystal defects, optical and optoelectronic properties of ZnO: CeO₂ mixed oxide thin films. *Photonics* **7**(4), 112 (2020)
45. M. De, S.S. Gupta, Lattice imperfection studies in polycrystalline materials by X-ray diffraction line-profile analysis. *Pramana* **23**(6), 721–744 (1984)
46. B.E. Warren, Addison Wesley Publishing. Co., London 18 (1969)
47. E. Deligoz, K. Colakoglu, Y. Ciftci, Elastic, electronic, and lattice dynamical properties of CdS, CdSe, and CdTe. *Phys. B: Condens. Matter* **373**(1), 124–130 (2006)
48. A.A. Akl, S.A. Mahmoud, S. Al-Shomar, A. Hassanien, Improving microstructural properties and minimizing crystal imperfections of nanocrystalline Cu₂O thin films of different solution molarities for solar cell applications. *Mater. Sci. Semiconduct. Process.* **74**, 183–192 (2018)
49. B. Warren, B. Averbach, The effect of cold-work distortion on X-ray patterns. *J. Appl. Phys.* **21**(6), 595–599 (1950)
50. D. Balzar, H. Ledbetter, Voigt-function modeling in Fourier analysis of size-and strain-broadened X-ray diffraction peaks. *J. Appl. Crystallogr.* **26**(1), 97–103 (1993)
51. E. Rabani, An interatomic pair potential for cadmium selenide. *J. Chem. Phys.* **116**(1), 258–262 (2002)
52. V. Mote, Y. Purushotham, B. Dole, Williamson-Hall analysis in estimation of lattice strain in nanometer-sized ZnO particles. *J. Theor. Appl. Phys.* **6**(1), 1–8 (2012)
53. A.A. Akl, A. Hassanien, Microstructure and crystal imperfections of nanosized Cd_xS_{1-x} thermally evaporated thin films. *Superlattices Microstruct.* **85**, 67–81 (2015)
54. G. Williamson, R. Smallman, III. Dislocation densities in some annealed and cold-worked metals from measurements on the X-ray debye-scherrer spectrum. *Philos. Mag.* **1**(1), 34–46 (1956)
55. A. Ahmad, A. Alsaad, Q. Al-Bataineh, M. Al-Naafa, Optical and structural investigations of dip-synthesized boron-doped ZnO-seeded platforms for ZnO nanostructures. *Appl. Phys. A* **124**(6), 458 (2018)
56. A.A. Ahmad, M.H. Khazaleh, A.M. Alsaad, Q.M. Al-Bataineh, A.D. Telfah, Characterization of As-prepared PVA-PEO/ZnO-Al₂O₃-NPs hybrid nanocomposite thin films. *Polym. Bull.* (2021). <https://doi.org/10.1007/s00289-021-03969-3>
57. P. Norouzzadeh, K. Mabhouti, M. Golzan, R.J.O. Naderali, “Investigation of structural, morphological and optical characteristics of Mn substituted Al-doped ZnO NPs: a Urbach energy and Kramers-Kronig study. *Optik* **204**, 164227 (2020)
58. R. Bhajantri, V. Ravindrachary, A. Harisha, C. Ranganathiah, G. Kumaraswamy, Effect of barium chloride doping on PVA microstructure: positron annihilation study. *Appl. Phys. A* **87**(4), 797–805 (2007)
59. A.S. Hassanien, A.A. Akl, Effect of Se addition on optical and electrical properties of chalcogenide CdSSe thin films. *Superlattices Microstruct.* **89**, 153–169 (2016)
60. Q.M. Al-Bataineh, A.A. Ahmad, A. Alsaad, A.D.J.H. Telfah, Optical characterizations of PMMA/metal oxide nanoparticles thin films: bandgap engineering using a novel derived model. *Heliyon* **7**(1), e05952 (2021)
61. G. Veena, B. Lobo, AC and DC electrical transport properties of potassium permanganate doped PVA-PVP solid polymer electrolyte. *Mater. Res. Express* **6**(3), 035315 (2018)

Publisher's Note Springer Nature remains neutral with regard to jurisdictional claims in published maps and institutional affiliations.